Fuel Processing Technology 162 (2017) 45–54

Contents lists available at ScienceDirect

Fuel Processing Technology

journal homepage: www.elsevier.com/locate/fuproc

Research article

Preparation of porous carbons from waste sugar residue for high performance electric double-layer capacitor

Zhi-Qiang Hao [a], Jing-Pei Cao [a,*], Yan Wu [a], Xiao-Yan Zhao [a,*], Li Zhou [b], Xing Fan [a], Yun-Peng Zhao [a], Xian-Yong Wei [a]

[a] Key Laboratory of Coal Processing and Efficient Utilization (Ministry of Education), China University of Mining & Technology, Xuzhou 221116, Jiangsu, China
[b] Department of Chemistry and Chemistry Engineering, Zaozhuang University, Zaozhuang 227132, Shandong, China

ARTICLE INFO

Article history:
Received 28 December 2016
Received in revised form 27 March 2017
Accepted 27 March 2017
Available online 1 April 2017

Keywords:
Waste sugar residue
Porous carbon
Electric double-layer capacitor
Capacitance
Cycle lifetime

ABSTRACT

Waste sugar solution is harmful to the environment and abundant in organic waste, and waste sugar residue (WSR) was obtained by drying waste sugar solution. In order to efficiently solve this issue and created values, activated carbon was prepared by WSR with KOH as activation agent. Carbonization temperature, activation temperature, activation ratio and activation time were investigated, based on the effects of preparation conditions on the electrochemical performance of activated carbon. The electrode material shows superior electrochemical performance, especially when the activated carbon was prepared at the carbonization temperature of 600 °C, activation temperature of 700 °C, activation ratio of 3:1 (KOH:char) and activation time of 2.5 h. It possesses the optimal electrochemical performance with a specific capacitance of 273.31 F g^{-1} and a specific surface area of 1953 m^2 g^{-1}. In order to determine the electrochemical stability of activated carbon electrodes, the cycle lifetime was performed at a current density of 1.5 A g^{-1}. After 5000 cycles, the capacitance retention rate of 90.1% could be obtained. Additionally, the energy density was relatively high at 1.5 A g^{-1} (up to 5.09 Wh kg^{-1}). This study provides a value-added approach for WSR treatment and a potential feedstock for low cost-high performance activated carbons for electric double-layer capacitor.

1. Introduction

In modern society, limited fossil fuel energy and serious greenhouse effect have prompted researchers to develop a kind of efficient, economical and green energy storage device [1–3]. Electric double-layer capacitor (EDLC) is considered to be one of the most potential energy storage devices. Taking advantage of the charge separation in a Helmholtz double layer at the interface between the electrolyte and electrode, EDLC possesses the advantages of superior electrochemical performance, environmentally-friendly products and long cycle life [4–6]. It is well known that the electrochemical performances of EDLC are basically determined by the kind of electrode active materials which include activated carbon (AC) [7], carbon nanotube [8], carbon aerogel [9] and graphene [10]. AC is a relatively inexpensive and high-performance electrode material and also has porous structure, large specific surface area (SSA), variable characteristics of surface chemistry and excellent surface reactivity [11]. Meanwhile, it can be prepared by various raw materials, such as coal, coconut shell, fruit shell and biomass [12–15]. AC as the most successful electrode material in the commercialization, many electrochemical workers have focused on the exploration of new precursors via adopting different activation agents (KOH, H_2SO_4 and $ZnCl_2$) to prepare AC with extraordinary performance for EDLC [16–18]. Zhai et al. [19,20] used mesophase pitch to prepare ACs with KOH as activation agent and found the AC with SSA of 2258 m^2 g^{-1}. When AC was applied in the supercapacitors, it had the largest specific capacitance of 145 F g^{-1} in organic electrolytes as well as high energy density of 31 Wh kg^{-1} and power density of 12 kW kg^{-1}. Wu et al. [21] used enteromorpha overrunning in China Sea as precursor to prepare porous carbons with the activation agent of $ZnCl_2$. The specific capacitance reached 206 F g^{-1}, and 93% of the initial specific capacitance was retained even after 5000 cycles. Furthermore, the carbon precursor was activated by KOH, which is more efficient in activating precursor with higher SSA and more controllable pore size distribution, compared with H_2SO_4, $ZnCl_2$ and NaOH [22].

Recycling waste material not only can ease the energy crisis, can also adjust the energy resource structure and environment protection. Moreover, the process of manufacturing vitamin C resulted in the production of high concentrations of waste sugar solution (WSS), which contains various waste materials, such as waste acids and organics, and it will pollute the environment and waste the recyclable resource

* Corresponding authors.
E-mail addresses: caojingpei@cumt.edu.cn (J.-P. Cao), zhaoxiaoyan@cumt.edu.cn (X.-Y. Zhao).

http://dx.doi.org/10.1016/j.fuproc.2017.03.031
0378-3820/

if discharged directly. In addition, WSS is generally used for the production of low value-added products, such as oxalate and detergent. Waste sugar residue (WSR) obtained by drying WSS can be used to prepare porous carbon, which has not been reported until now. Hence, it is significant and necessary to prepare high value-added item like porous AC based electrodes by recycling WSR. It is feasible for WSR to prepare ACs because of its low ash content and abundant elemental contents of C and O which are conducive to increase the electrochemical performance of ACs [23]. Besides, relatively high alkali metal content in WSR is beneficial to activation by the reduce of the application amount of activation agent to some extent [24].

In this study, WSR was favorable to be the precursor for the preparation of ACs with KOH as activation agent applied in EDLC. The prepared ACs were characterized by Fourier transform infrared (FTIR) spectrometer, scanning electron microscopy (SEM), X-ray diffraction (XRD) and N_2 adsorption-desorption. Subsequently, the electrochemical performances of AC based electrodes were investigated by galvanostatic charge-discharge (GCD), cyclic voltammetry (CV) and electrochemical impedance spectroscopy (EIS) measurements. This paper focuses on the effects of carbonization temperature, activation temperature, activation ratio and activation time on the electrochemical performance of ACs prepared by WSR.

2. Experimental

2.1. Material

The WSS, collected from vitamin C pharmaceutical company in Shandong, China, was dried at 105 °C in the oven for 12 h and the dried WSR was pulverized to pass through a 200-mesh sieve followed by drying at 105 °C for 12 h. Ultimate analysis was carried out by an Elementar vario MACRO cube CHNS elemental determinator [25]. The main characteristics of the WSR are shown in Table 1. Thermodynamic property of WSR was investigated and the thermogravimetry (TG) and derivative thermogravimetry (DTG) are listed in Supplementary material.

2.2. Preparation and characterization of ACs

The AC was prepared by two-step carbonization/KOH-activation method under Ar flow at a fixed heating rate of 10 °C min^{-1} via WSR as the precursor.

Step 1 (carbonization), WSR was carbonized for 2 h at various carbonization temperatures for the preparation of char. Step 2 (KOH-activation), char was activated at various activation temperatures, activation ratios (KOH: char) and activation times. Then, the samples were rinsed with 2 M HCl solution and sufficient deionized water until neutral. Finally, the washed samples were dried at 150 °C for 3 h in a vacuum drying oven. The prepared ACs were designated on the basis of the naming rule: AC-*w*-*x*-*y*-*z* (w = 500, 600, 650 and 700, referring to the carbonization temperature of 500, 600, 650 and 700 °C, respectively; x = 500, 600, 700 and 800, referring to the activation temperature of 500, 600, 700 and 800 °C, respectively; y = 1, 2, 3 and 4, referring to the activation ratio of 1:1, 2:1, 3:1 and 4:1, respectively; z = 1.5, 2, 2.5 and 3, referring to the activation time of 1.5, 2, 2.5 and 3 h, respectively). The schematic illustration of the preparation process of ACs is shown in Fig. 1, and all the experimental data have been carried out in parallel.

Table 1
Proximate and ultimate analyses of WSR.

Proximate analysis (wt%)[a]			Ultimate analysis (daf, wt%)				
A_d	VM_d	FC_d[b]	C	H	N	O[b]	S
6.56	76.26	17.18	48.94	4.46	1.28	42.91	2.41

[a] A: ash; VM: volatile matter; FC: fixed carbon; d: dry basis; daf: dried and ash-free basis.
[b] Calculated by difference.

The functional groups on the surface of ACs were characterized by a Nicolet Corporation IR-560 FTIR spectrometer. A FEI Quanta TM 250 SEM was used to observe the surface morphology of the prepared samples. XRD analysis was performed on the Bruker D8 Advance X-ray diffractometer using Cu Kα radiation (λ = 0.15418 nm). The textural properties of the prepared ACs were tested by N_2 adsorption-desorption experiments at 77 K with a Quantachrome Autosorb-1 apparatus. Moreover, the Brunauer-Emmett-Teller (BET) method and Density Functional Theory (DFT) method were applied to reckon the SSA and the pore size distribution, respectively.

2.3. Fabrication of ACs electrodes and EDLCs

For the fabrication of AC electrodes, the AC (87 wt%) was homogeneously mixed with acetylene black (10 wt%) and polytetrafluoroethylene (PTFE, 3 wt%) in agate mortar [26]. Secondly, the mixture was grinded to half dry state and then was pressed onto the nickel foam which was used as a current collector with 13 mm diameter under a certain pressure for the preparation of electrode. Subsequently, electrodes were immersed in a 6 M KOH solution (24 h) which was used as electrolyte.

EDLC was assembled by two electrodes and a polymer separator in a MTI Corporation EQ-STC split test cell, and two electrodes were separated by polymer separator wetted with the 6 M KOH solution.

2.4. Electrochemical measurements

GCD, CV and EIS measurements are needed to be tested for the investigation of the electrochemical performance of EDLCs. GCD curves were recorded at current densities between 40 and 200 mA g^{-1} within the potential window of 0 to 0.9 V by a NEWARE CT-3008-5V50mA-164 battery testing system. The mass specific capacitance (C_S, F g^{-1}) of a single electrode is calculated by the slope of discharge curves, as the following equation [27]:

$$C_S = \frac{2I\Delta t}{m\Delta V} \quad (1)$$

where I (A) represents current, Δt (s) represents the time of discharge, m (g) represents the mass of single electrode, and ΔV (V) represents the drop of potential in Δt. An Iviumstat Vertex electrochemical workstation was used to assess CV and EIS. CV profiles were recorded between 0 and 1 V at different potential sweep rates. EIS was accomplished by a frequency range from 10 kHz to 10 mHz at open circuit voltage with amplitude of 10 mV.

3. Results and discussion

3.1. Characterization of ACs

The proximate analysis of WSR and the yields of carbonization and activation are listed in the Tables 1 and 2. WSR has relatively low ash content, and its carbonization and activation yields are comparable to the carbonization and activation yields of rice husk and peanut shell [28,29]. Besides, the computational equations of the yields of carbonization and activation are listed in the Supplementary material.

In order to figure out the changes of the surface functional groups, we characterized the WSR, char and AC-600-700-3-2.5 by FTIR spectrometer. As shown in Fig. 2, the peak at 3434 cm^{-1} is assigned to the stretching vibration of –OH stem from adsorbed water molecules and structural hydroxyl groups [30,31]. The weak peaks at 2920 and 1410 cm^{-1} of AC-600-700-2.5 can represent C-H stretching and -COO- symmetrical stretching vibration, respectively. The peaks around 1061–948 cm^{-1} represent hydroxyl stretching vibration in olefin and

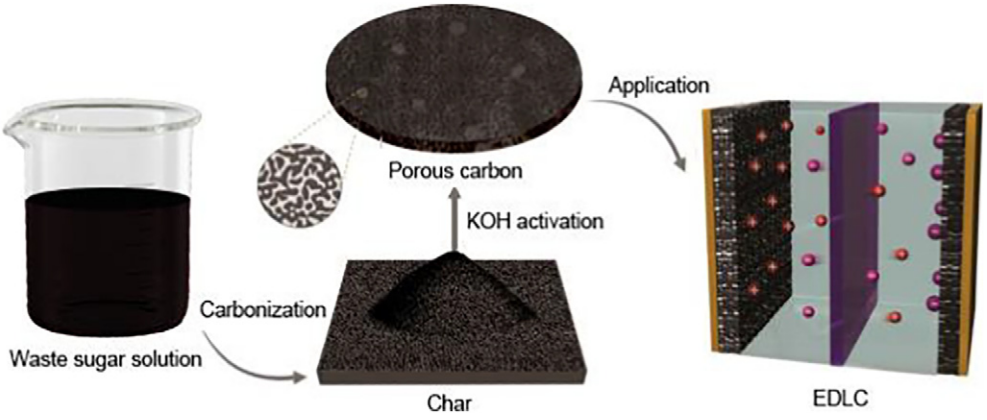

Fig. 1. Schematic illustration of the preparation process of ACs.

aromatic ring, while the bands at 1620 cm^{-1} are contributed to C=C stretching vibration in aromatic ring [6]. Before and after activation, the main change is the appearance of oxygen-containing functional groups (-COO- at 1410 cm^{-1} and –OH at 963 cm^{-1}), which might lead to the improvement of wettability and the formation of pseudocapacitance, and as a result leads to the enhancement of the electrochemical performance of AC, as reported by [12,32].

The char and AC-600-700-3-2.5 were verified by SEM in order to observe the textural transformation of the samples after activation. According to the SEM images (Fig. 3) and the N_2 adsorption-desorption results of char (Fig. S1 and Table S1), the surface of char is rough and the adsorption volume of char is small. By contrast, AC-600-700-3-2.5 possesses not only smooth surface, but also porous structure, which are beneficial to the diffusion of electrolyte ion from the electrolyte to the electrode interface due to the developed porous structure [33,34].

As shown in Fig. 4, there is a (100) diffraction peak at 2θ angle of 43.5° in the XRD pattern of AC-600-700-3-2.5, which demonstrates that AC-600-700-3-2.5 possesses amorphous character and consists of diminutive areas of ordered graphene sheets [35,36]. The AC-600-700-3-2.5 has considerable intensity in the low-angle scatter because it presents developed pore structure [37].

3.2. Effect of carbonization temperature

The carbonization temperature has a great influence on the electrochemical performance of ACs, and the main purpose of carbonization is to promote the content of carbon and the porosity of char which is mainly due to the release of volatiles from WSR [38]. As shown in Fig. S2, the main stage of weight loss is between 200 °C and 500 °C. Meanwhile, DTG curve shows that a peak appeared at 210 °C. This is because a large number of unstable volatiles began to release. Still 40% of the WSR remains in char at 900 °C and the weight loss rate is slowly above 500 °C, indicating that WSR has superior thermal stability and volatile matters were almost completely released after 500 °C. Hence, the range of carbonization temperature could be chosen from 500 to 700 °C. The isotherm of AC-*w*-700-3-2 in Fig. 5a is allocated to type I (AC-500-700-3-2) and type IV (AC-600-700-3-2, AC-650-700-3-2 and AC-700-700-3-2) according to IUPAC classification [39], indicating the presence of micropores and mesopores, which also could be determined through Fig. 6a and Table 2. In the N_2 adsorption-desorption isotherms, the increase of adsorbed volume is correlated with micropores at the relative pressure (P/P_0) from 0 to 0.4. The hysteresis loops reveal the presence of mesopores at medium P/P_0 from 0.4 to 0.9 and the presence of macropores could be demonstrated by the tail of isotherms at the high P/P_0 (~1.0) [40]. In addition, mesopores have a beneficial effect on decreasing ion-transport resistance, and micropores are propitious to increase specific capacitance because micropores possess a great deal of adsorption sites [41]. As outlined in Table 2, AC-600-700-3-2 possesses the highest SSA of 1796 $m^2\ g^{-1}$.

Fig. 7a and b show that the GCD curve of AC-*w*-700-3-2 has the features of symmetric triangular and approximately straight line at a current density of 40 mA g^{-1}, indicating that AC-*w*-700-3-2 has good

Table 2
The characterization of all samples.

Sample	S_{BET}[a] ($m^2\ g^{-1}$)	S_{micro}[b] ($m^2\ g^{-1}$)	S_{meso}[c] ($m^2\ g^{-1}$)	V_{tot}[d] ($cm^3\ g^{-1}$)	V_{micro}[b] ($cm^3\ g^{-1}$)	V_{meso}[c] ($cm^3\ g^{-1}$)	D[e] (nm)	Y_c[f] (%)	Y_a[f] (%)
AC-500-700-3-2	1326	1267	59	0.741	0.523	0.218	2.24	41.7	51.5
AC-600-700-3-2	1796	1707	89	0.810	0.702	0.108	1.80	39.6	53.2
AC-650-700-3-2	1346	1152	193	0.743	0.496	0.247	2.21	38.6	54.3
AC-700-700-3-2	1531	1447	85	0.755	0.577	0.178	1.97	37.9	56.0
AC-600-500-3-2	803	720	83	0.437	0.296	0.141	2.17	39.6	65.2
AC-600-600-3-2	1206	1121	85	0.564	0.445	0.119	1.87	39.6	63.6
AC-600-800-3-2	1425	1262	163	0.755	0.537	0.218	2.12	39.6	47.6
AC-600-700-1-2	818	690	128	0.567	0.320	0.247	2.77	39.6	68.0
AC-600-700-2-2	960	839	121	0.568	0.354	0.214	2.37	39.6	57.3
AC-600-700-4-2	1615	1480	135	0.771	0.616	0.155	1.91	39.6	38.7
AC-600-700-3-1.5	1529	1433	96	0.724	0.596	0.128	1.89	39.6	54.2
AC-600-700-3-2.5	1953	1821	132	0.922	0.766	0.156	1.89	39.6	47.6
AC-600-700-3-3	1781	1659	121	0.892	0.706	0.186	2.00	39.6	43.1

[a] S_{BET}: specific surface area from multiple BET method.
[b] S_{micro}, V_{micro}: micropore surface area and micropore volume.
[c] S_{meso}, V_{meso}: mesopore surface area and mesopore volume.
[d] V_{tot}: total pore volume at $P/P_0 = 0.99$.
[e] D: average pore diameter.
[f] Y_c, Y_a: char yield and AC yield.

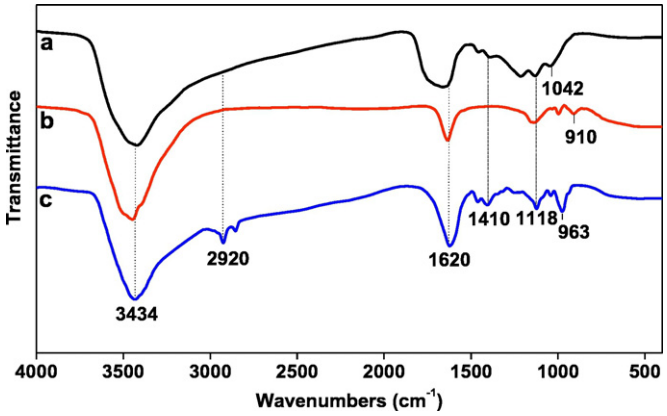

Fig. 2. FTIR spectra of WSR (a), char (b) and AC-600-700-3-2.5 (c).

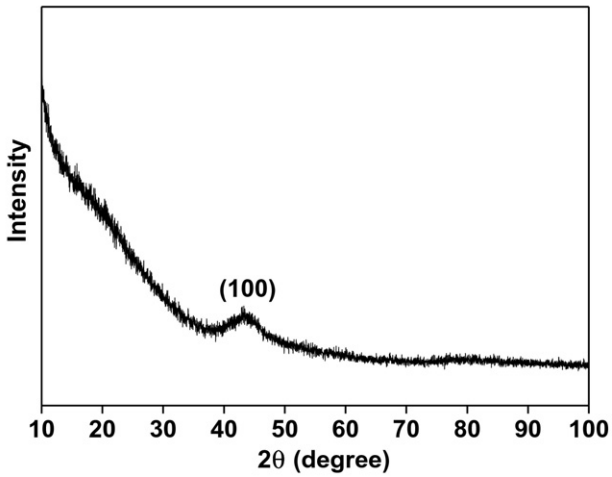

Fig. 4. XRD pattern of AC-600-700-3-2.5.

electrochemical reversibility. In addition, Fig. 7c shows that the samples present rectangle shapes, exhibiting a quick charge propagation capability.

Based on Fig. 7b and Eq. (1), the specific capacitance was calculated that AC-600-700-3-2 possesses the largest specific capacitance of 266.47 F g^{-1}. Meanwhile, Fig. 7c also shows the change of specific capacitance at different carbonization temperatures since the area of CV curve is proportional to specific capacitance. This results from the fact that the SSA of AC-600-700-3-2 is the largest when carbonization temperature was changed. However, the SSA of AC-700-700-3-2 is larger than AC-650-700-3-2 while the specific capacitance of AC-650-700-3-2 is higher than AC-700-700-3-2. This is because more volatile was released from WSR and more micropores were produced when the carbonization temperature increased from 600 to 700 °C, according to Li et al. [38]. The micropores, produced by carbonation and activation, were etched into mesopores by KOH. Microporous structure is easily damaged, and the degree of etching of some micropores is not serious because the number of micropores in the char is relatively high. The micropore surface area and SSA of AC-700-700-3-2 are larger than AC-650-700-3-2 due to its relatively high microporosity. Additionally, the micropore surface area and SSA of AC-600-700-3-2 are larger than others, which should be due to the reaction of char (carbonized at 600 °C) with KOH and the generation of a great deal of new micropores. The micropore surface area and SSA of AC-500-700-3-2 are the smallest which should be because excessive KOH enlarged the pore size, resulting in the decrease in surface area and the increase in average pore diameter (2.24 nm), as listed in Table 2. Nevertheless, as shown in Fig. 6a, the micropores size distribution of AC-700-700-3-2 concentrated in 0.9 nm (<1 nm) which was too small to be advantageous for ion transfer [42]. Moreover, the SSA of AC-600-700-3-2 was larger than AC-700-700-3-2, and the average pore diameters of AC-600-700-3-2 and AC-700-700-3-2 are approximately equal (1.80 nm vs. 1.97 nm). Therefore, the specific capacitance of AC-600-700-3-2 is higher than AC-650-700-3-2 and AC-700-700-3-2. Meanwhile, the optimal carbonization temperature (600 °C) was initially determined.

3.3. Effect of activation temperature

According to the discussion above, the effect of activation temperature is immediately discussed in this section. The isotherm of AC-600-*x*-3-2 belongs to type I in Fig. 5b, which shows that the micropores dominate in the pore size distribution of AC-600-*x*-3-2. As illustrated by Table 2 and Fig. 6b, the SSA of AC-600-*x*-3-2 is mainly contributed from micropores. The SSA of AC-600-*x*-3-2 increased from 803 to 1796 m^2 g^{-1} when raising activation temperature from 500 to 700 °C and then decrease to 1425 m^2 g^{-1} by further raising activation temperature from 700 to 800 °C. It should be due to the increase of activation temperature can enhance the degree of activation, which leads to the increase of SSA. However, excessive activation temperature will cause partial micropores collapse to mesopores, resulting in the decrease of SSA and total pore volume [43]. Thereby, the SSA and total pore volume of AC-600-700-3-2 (1769 m^2 g^{-1} and 0.810 cm^3 g^{-1}) are larger than AC-600-500-3-2, AC-600-600-3-2 and AC-600-800-3-2.

As shown in Fig. 8a, the GCD curves of AC-600-700-3-2 and AC-600-800-3-2 assume symmetric triangular shapes and high linearity,

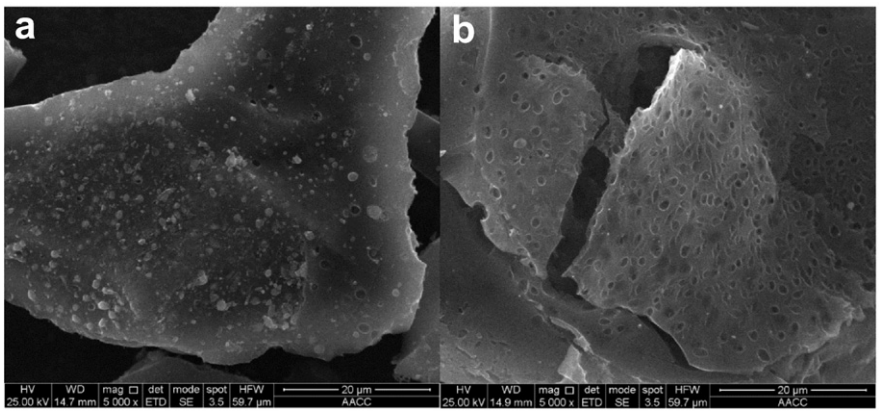

Fig. 3. SEM images of char (a) and AC-600-700-3-2.5 (b).

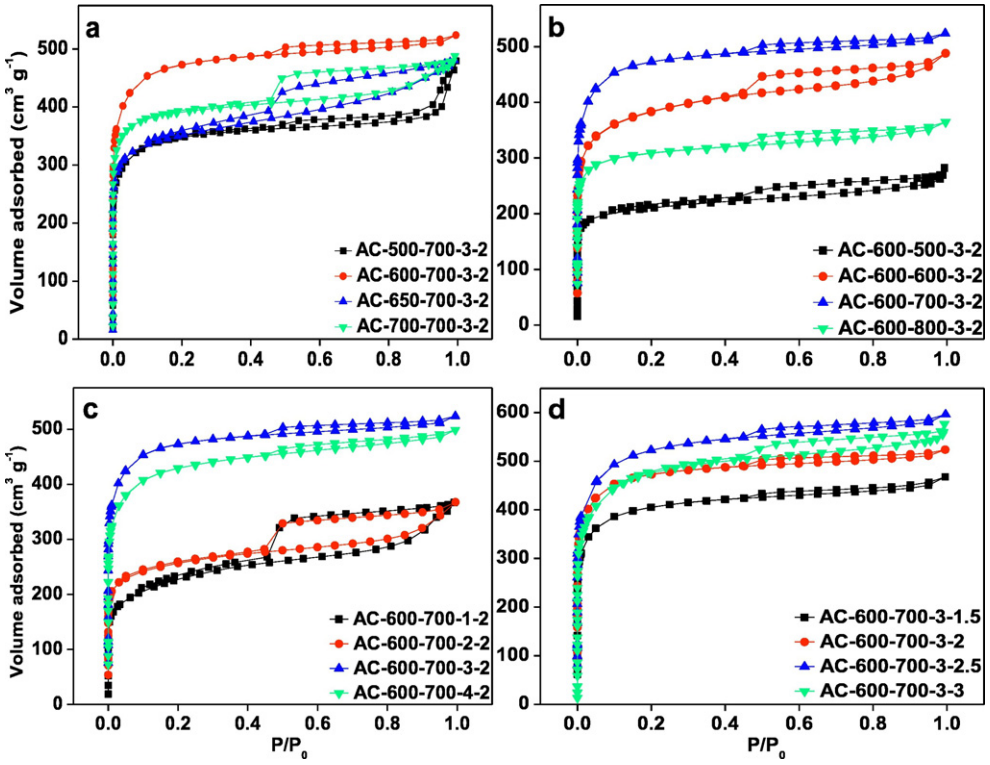

Fig. 5. Nitrogen adsorption-desorption isotherms of the prepared ACs at different carbonization temperatures (a), activation temperatures (b), activation ratios (c) and activation times (d).

indicating ideal EDLC behaviors. AC-600-700-3-2 has the highest specific capacitance of 266.47 F g^{-1} at a current density of 40 mA g^{-1} according to Eq. (1). The CV curve of AC-600-*x*-3-2 at the scan rate of 2 mV s^{-1} is illustrated in Fig. 8b. At the designated voltage scope from 0 to 1 V, these curves have approximately rectangular shapes (AC-600-700-3-2 and AC-600-800-3-2), suggesting that they possess approximately ideal electrochemical reversibility [44]. The CV curve area of AC-600-700-3-2 is larger than AC-600-500-3-2, AC-600-600-3-2 and AC-800-

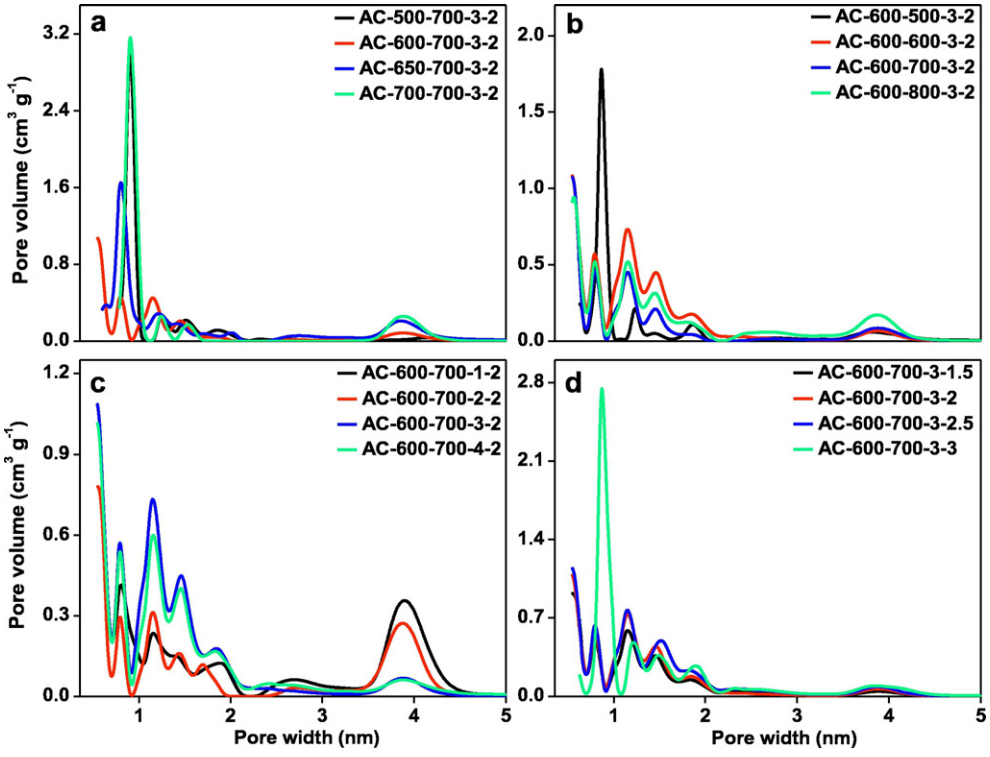

Fig. 6. Pore size distribution of the prepared ACs at different carbonization temperatures (a), activation temperatures (b), activation ratios (c) and activation times (d).

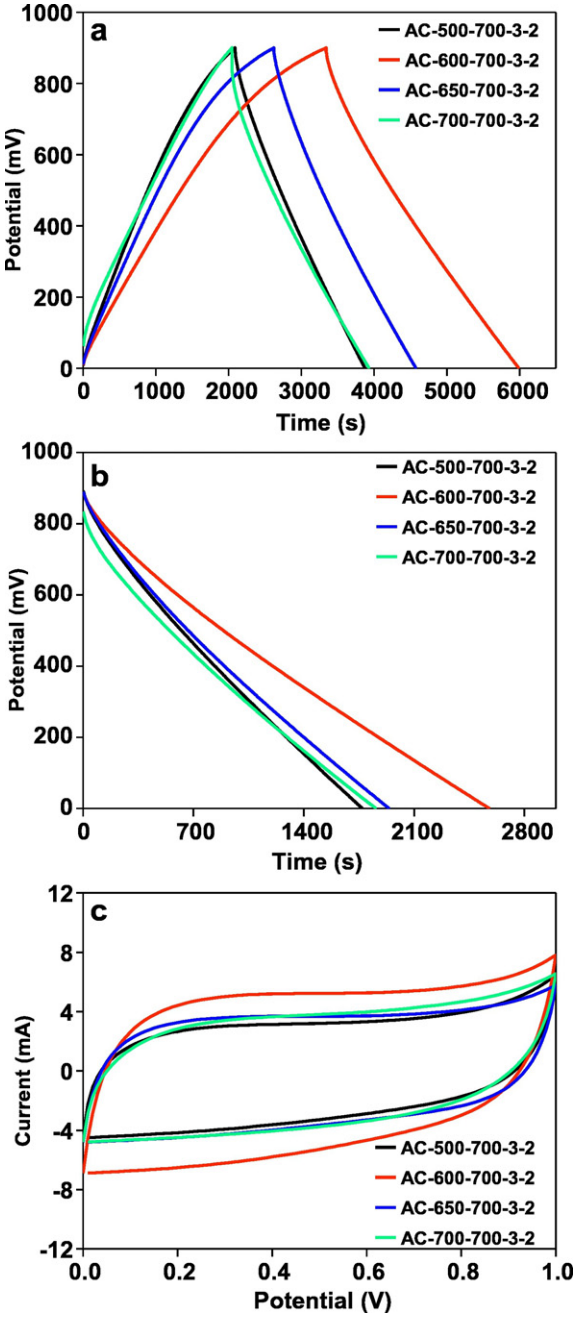

Fig. 7. GCD curve of AC-*w*-700-3-2 at 40 mA g^{-1} (a); discharge curve of AC-*w*-700-3-2 at 40 mA g^{-1} (b); CV curve of AC-*w*-700-3-2 at the scan rate of 2 mV s^{-1} (c).

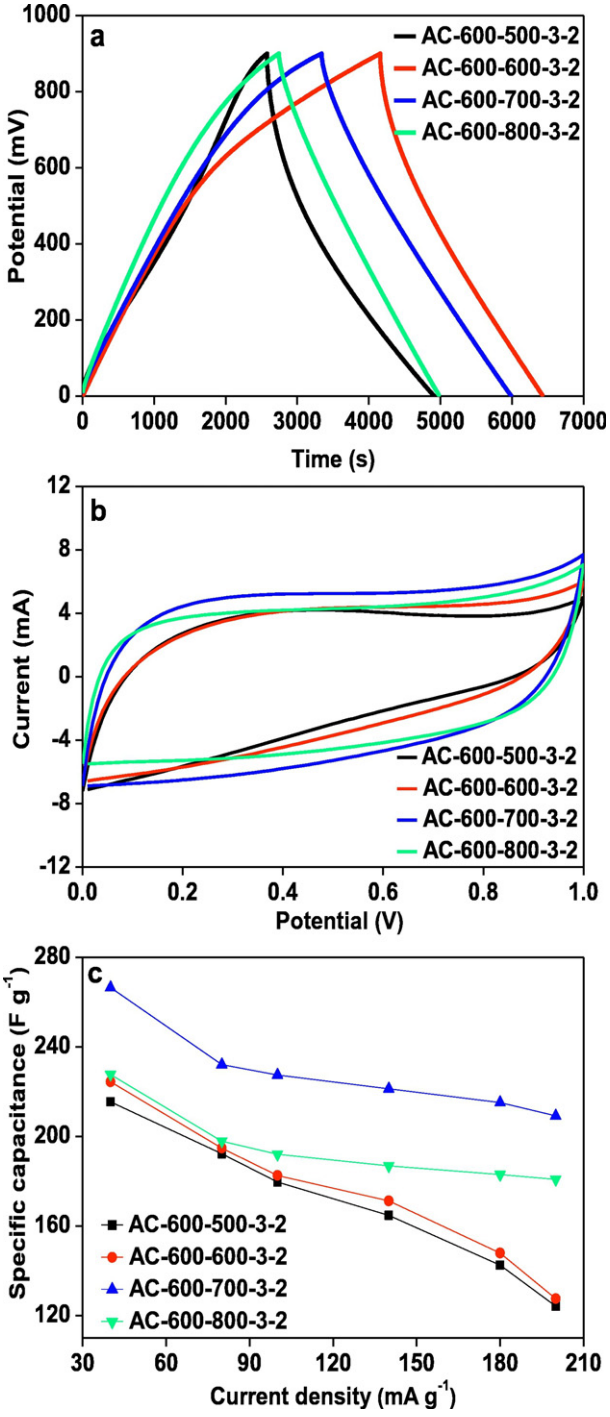

Fig. 8. GCD curve of AC-600-*x*-3-2 at 40 mA g^{-1} (a); CV curve of AC-600-*x*-3-2 at the scan rate of 2 mV s^{-1} (b); the specific capacitance of AC-600-*x*-3-2 at varied current densities (c).

3-2, which could also prove that AC-600-700-3-2 possesses higher specific capacitance. However, the GCD and CV profiles of AC-500-600-3-2 and AC-600-600-3-2 deformed from the standard shape, which may present relatively high internal resistance (IR) due to low activation temperature [43].

From Fig. 8c, the specific capacitance of AC-600-*x*-3-2 decreased with the increase of current density, which could be assigned to the rapid diffusion of ions between the interface of electrolyte and electrode during the charge-discharge process, and the speed of diffusion is faster at higher current density [40]. It is visible that AC-600-700-3-2 has higher specific capacitance and smaller attenuation degree of specific capacitance than AC-600-500-3-2, AC-600-600-3-2 and AC-600-800-3-2, with the increase of current density. The specific capacitance of AC-600-700-3-2 is 266.47 F g^{-1} at 40 mA g^{-1}. Moreover, AC-600-700-3-2 still possesses the specific capacitance of 209.24 F g^{-1} at a higher current density of 200 mA g^{-1}, indicating an excellent ion-diffusion ability of AC-600-700-3-2 [45]. These results are mainly due to the SSA and pore size distribution: (1) AC-600-700-3-2 has a relatively high effective SSA, compared with AC-600-500-3-2, AC-600-600-3-2 and AC-600-800-3-2 (Table 2); (2) The pore structure of AC-600-700-3-2 is advantageous to transport electrolyte ion due to the relatively suitable pore size distribution [46]. Therefore, the prepared AC has excellent electrochemical performance at the activation temperature of 700 °C when activation temperature was changed.

3.4. Effect of activation ratio

It is common knowledge that the activation ratio is one of the most important factors in chemical activation. The activation ratio was modified to find the best electrochemical performance when carbonization temperature, activation temperature and activation time were fixed at 600 °C, 700 °C and 2 h, respectively. From Figs. 6c, 5c and Table 2, it can be seen that type I isotherms are observed and with the increase of activation ratio from 2:1 to 3:1, the SSA of AC-600-700-*y*-2 increased from 818 to 1796 $m^2 g^{-1}$ and then decreased from 1796 to 1615 $m^2 g^{-1}$ when activation ratio was further increased. Additionally, the SSA is mainly from the contribution of micropores. The reasons for this trend should be a small quantity of KOH results in incomplete activation and superfluous KOH causes some micropores etched into mesopores [47].

It is clearly shown in Fig. 9a that the curve of AC-600-700-*y*-2 is almost symmetric and linear, which has ideal nature of EDLC. Additionally, the specific capacitance could be calculated through the slopes of discharge curves, indicating that AC-600-700-3-2 has the highest specific capacitance compared with AC-600-700-1-2, AC-600-700-2-2 and AC-600-700-4-2, corresponding to their SSAs. The integral area of CV curves in Fig. 9b can further prove this conclusion and no pronounced redox peaks can be discovered in the CV curves, indicating that the specific capacitance is mainly composed of electric double-layer capacitance and scarcely contains pseudocapacitance [48], despite the presence of -COO- species. This is might be because the content of generated oxygen-containing functional groups was small when AC was activated with KOH, resulting in the phenomenon of little pseudocapacitance. AC-600-700-3-2 possesses prominent electrical conductivity, which can be revealed from Fig. 9c. Moreover, its specific capacitance at the current density of 200 mA g^{-1} still maintains 79% of the initial specific capacitance at the current density of 40 mA g^{-1}, and the reduce rate is not obvious in comparison to AC-600-700-1-2, AC-600-700-2-2 and AC-600-700-4-2. From Fig. 9d, it could be observed that the CV profile gradually deviates from the standard rectangular shape with the increase of potential scan rate owing to polarization. In addition, electrolyte ion cannot diffuse into the inside of electrodes at a high potential scan rate in a short time and IR exists in the EDLCs. Therefore, the specific capacitance gradually decreased with the increase of the scan rate [49,50]. From the above analyses, the optimal activation ratio is 3:1 when char was activated at 700 °C for 2 h.

3.5. Effect of activation time

The optimal preparation conditions are roughly determined by changing carbonization temperature (600 °C), activation temperature (700 °C) and activation ratio (3:1). Hence, the activation time was measured for 1.5, 2, 2.5 and 3 h. The N_2 adsorption-desorption curve and pore size distribution of AC-600-700-3-*z* are shown in Figs. 5d and 6d, respectively. The isotherm of AC-600-700-3-*z* is apparently assigned to type I, and the details of the texture properties of the porous carbons are listed in Table 2. The SSA of AC-600-700-3-*z* increased with the increase of activation time, and AC-600-700-3-2.5 has the largest SSA of 1953 $m^2 g^{-1}$ and an average pore size of 1.89 nm. However, the excessive activation time (3 h) might lead to the collapse of the porous structure of AC-600-700-3-*z*, resulting in the occlusion of micro and mesopores. Consequently, the SSA decreased to 1781 $m^2 g^{-1}$.

It could be observed in Fig. 10a and b that AC-600-700-3-2.5 has the highest specific capacitance of 273.31 F g^{-1} based on the slopes of discharge curves and the area of CV curves. This is because AC-600-700-3-2.5 has a relatively high SSA (1953 $m^2 g^{-1}$) and the pore size distributions of AC-600-700-3-1.5, AC-600-700-3-2, AC-600-700-3-2.5 and AC-600-700-3-3 are similar (Fig. 6d). Meanwhile, AC-600-700-3-2.5 has typical charge-discharge characteristics of EDLCs since its GCD curve is visible regular triangular-shape and CV curve is approximately rectangular. These phenomena suggest that the electrode reaction is mainly the charge transfer on the double layer. The specific capacitances of AC-600-700-3-1.5, AC-600-700-3-2, AC-600-700-3-2.5 and AC-600-700-3-3 at various current

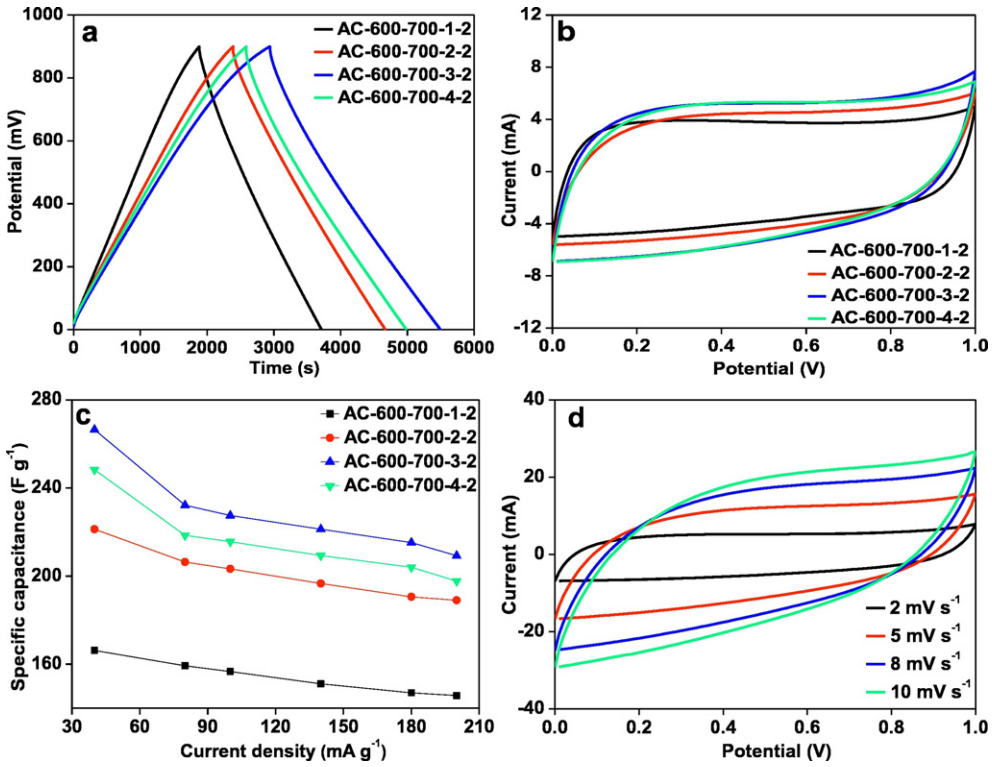

Fig. 9. GCD curve of AC-600-700-*y*-2 at 40 mA g^{-1} (a); CV curve of AC-600-700-*y*-2 at the scan rate of 2 mV s^{-1} (b); the specific capacitance of AC-600-700-*y*-2 at varied current densities (c); CV curves of the AC-600-700-3-2 sample at different scan rates (d).

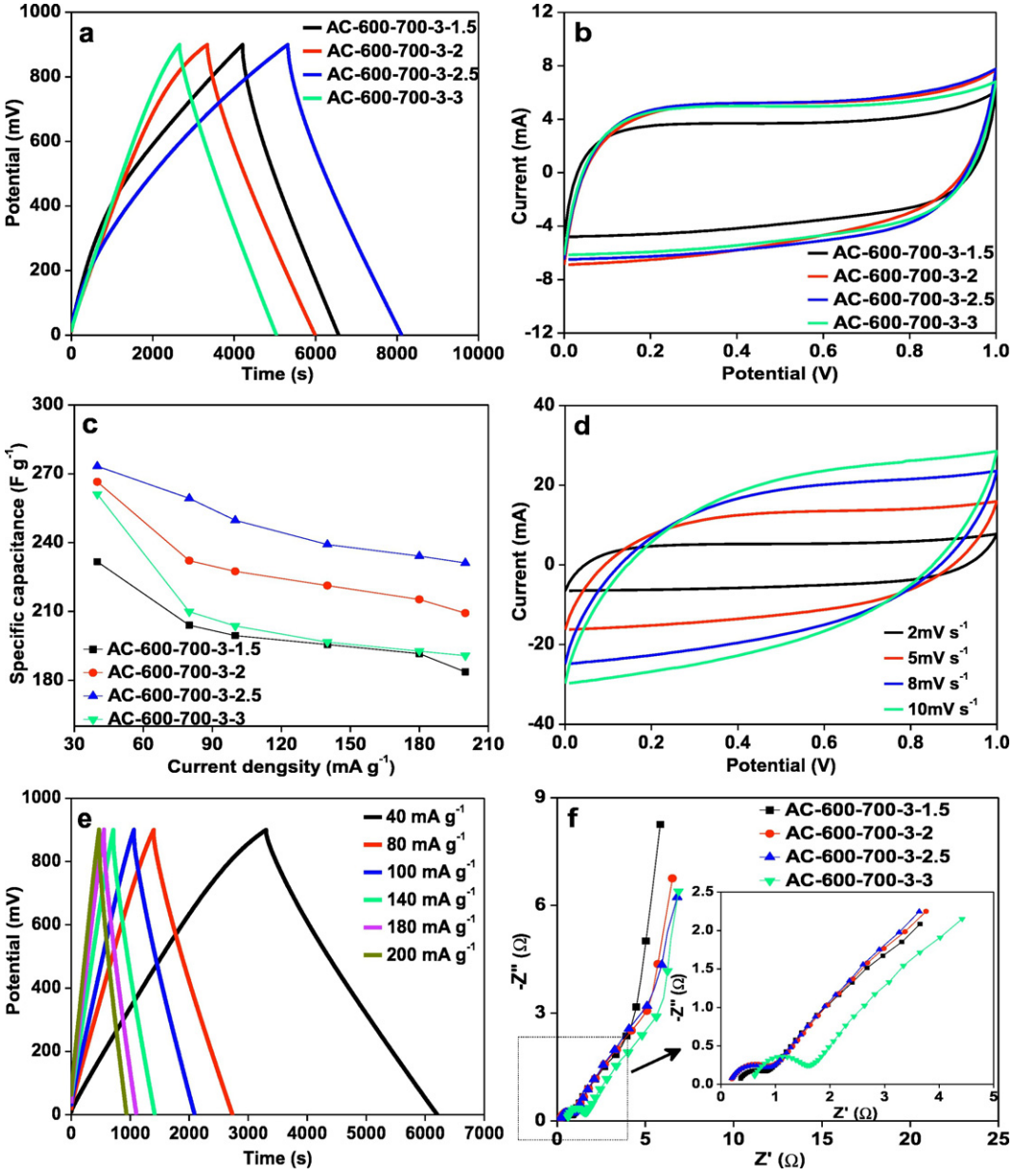

Fig. 10. GCD curve of AC-600-700-3-*z* at 40 mA g^{-1} (a); CV curve of AC-600-700-3-*z* at the scan rate of 2 mV s^{-1} (b); the specific capacitance of AC-600-700-3-*z* at varied current densities (c); CV curves of the AC-600-700-3-2.5 sample at different scan rates (d); GCD curves of AC-600-700-3-2.5 at different current densities (e); Nyquist plot of AC-600-700-3-*z* and the inset shows detail in the high-frequency range (f).

densities are listed in Fig. 10c. The specific capacitance of all samples decreased with the increase of current density. Among that, the attenuation degree of AC-600-700-3-2.5 is the slightest. In order to further confirm the electrochemical performance of AC-600-700-3-2.5, the CV measurements were measured at the potential range from 0 to 1 V at various scan rates. As shown in Fig. 10d, the deformation of CV curves became more and more serious and no visibly redox peaks appear with the increase of scan rates, implying comparatively ideal EDLC behavior. From Fig. 10e it can be observed that the GCD plots of AC-600-700-3-2.5 remain symmetric triangular shapes with the increase of current density, indicating the excellent ion diffusion and electron transport ability with the increase of current density [51]. No noticeable drop of IR can be found when the current density increased. This phenomenon reveals that the IR of AC-600-700-3-2.5 is low which resulted from excellent conductivity and good electrochemical reversibility [52,53].

The electrochemical performance of AC-600-700-3-*z* was measured by Nyquist plots and the results are shown in Fig. 10f. At the low frequency region, the curve of AC-600-700-3-*z* is nearly vertical line, owing to the diffusion of the electrolyte ions within the electrode structure, which also suggests that the electrode materials possess virtually ideal capacitive behavior [21,54]. Four semicircles could clearly be seen at the high frequency, and the intercept at the Z' axis represents the IR which is made up of the ionic resistance of the electrolyte, intrinsic resistance of the active materials and contact resistance with the current collector [55]. In addition, it is apparent that the IR of AC-600-700-3-1.5, AC-600-700-3-2, AC-600-700-3-2.5 and AC-600-700-3-3 are approximately equal. Besides, in the insert of Fig. 10f, the transfer resistance (R_{ct}) can be estimated by the size of semicircle at the high frequency region which is directly proportional to semicircle size, so that AC-600-700-3-2.5 has the smallest R_{ct} [56]. Warburg resistance (W) is determined by a slope of about 45° at the intermediate frequency

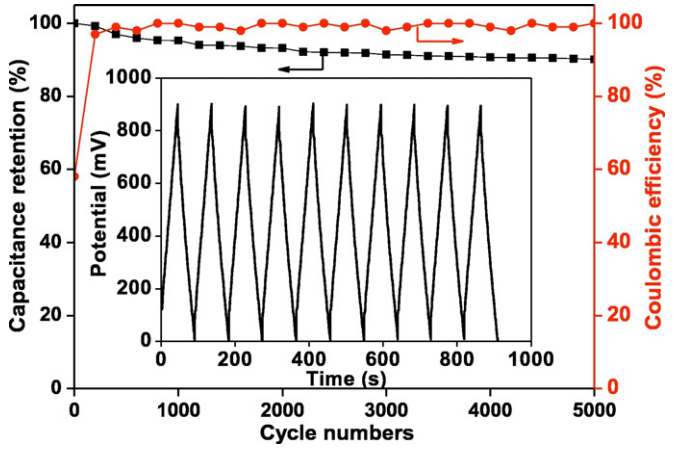

Fig. 11. The capacitance retention and coulombic efficiency of AC-600-700-3-2.5 at a current density of 1.5 A g^{-1} for 5000 cycles.

on the basis of the frequency dependence of ion diffusion when the ion is diffused from the electrolyte to the surface of electrode through the small pores [57]. The AC-600-700-3-2.5 has smaller resistance and better superior ion-diffusion performance than AC-600-700-3-1.5, AC-600-700-3-2 and AC-600-700-3-3.

For further estimate the practical application possibility of AC-600-700-3-2.5 as electrode material, the cycle performance of AC-600-700-3-2.5 was tested by GCD process at 1.5 A g^{-1} in 6 M KOH solution. After 5000 cycles, 90.1% of the initial specific capacitance was retained at 1.5 A g^{-1}, and the GCD plots still possessed highly symmetrical triangle shapes, as illustrated in Fig. 11 and the insert of Fig. 11. During the cycle life test, coulombic efficiency could reach 100%. The capacitance retention, however, decreased to 90.1%, which might be because pore structure was damaged in the process of cycle. In summary, AC-600-700-3-2.5 exhibits superior cycle stability and excellent electrochemical reproducibility, and it can be invoked as potential high performance electrode material [58,59].

The energy density (E), power density (P) and Coulomb efficiency (η) can be calculated via the following equations [60,61]:

$$E = \frac{1}{2}CU^2 \tag{2}$$

$$P = \frac{E}{t_1} \tag{3}$$

$$\eta = \frac{t_1}{t_2} \times 100\% \tag{4}$$

where C (F g^{-1}) is the specific capacitance, U (V) is the voltage scan range, t_1 (s) is discharge time and t_2 (s) is charge time. Depending on Fig. 11 and Eq. (2), the initial energy density of AC-600-700-3-2.5 is 5.09 Wh kg^{-1} at the current density of 1.5 A g^{-1}. Even after 5000 cycles, its energy density remains high value of 4.59 Wh kg^{-1}. As shown in Fig. S3, the current density was increased from 40 mA g^{-1} to 20 A g^{-1}. From the Ragone plot of AC-600-700-3-2.5, the highest energy density of 7.69 Wh kg^{-1} could be obtained at the current density of 40 mA g^{-1}, and the highest power density of 29.3 kW kg^{-1} could be obtained at the current density of 20 A g^{-1}. The relation of current density, power density and energy density is listed in Table S2. Hence, AC-600-700-3-2.5 has superior power density, which is comparable with [62].

4. Conclusions

In summary, porous carbons with a relatively high SSA of 1953 m^2 g^{-1} was obtained by two-step carbonization/KOH-activation method with WSR as raw material. The prepared ACs possessed the highest specific capacitance of 273.31 F g^{-1} at a current density of 40 mA g^{-1}. The capacity retention rate of AC-600-700-3-2.5 remained 90.1% after 5000 cycles, and its energy density reduced from 5.09 to 4.59 Wh kg^{-1} after 5000 cycles. Meanwhile, the excessive temperature, activation ratio and activation time were unfavorable for the electrochemical performance of the prepared ACs. The electrochemical performance of ACs not only related to the SSA, but also has a great relationship with pore size. Moreover, the WSR has an opportunity of being a potential and competitive precursor for the preparation of AC with excellent electrochemical properties.

Acknowledgements

This work was subsidized by the Fundamental Research Funds for the Central Universities (China University of Mining & Technology, 2015XKMS043), National Natural Science Foundation of China (Grant 21676292), Natural Science Foundation of Jiangsu Province (BK20161180), and the Priority Academic Program Development of Jiangsu Higher Education Institutions.

Appendix A. Supplementary data

Supplementary data to this article can be found online at http://dx.doi.org/10.1016/j.fuproc.2017.03.031.

References

[1] J. Wang, M. Chen, C. Wang, J. Wang, J. Zheng, Preparation of mesoporous carbons from amphiphilic carbonaceous material for high-performance electric double-layer capacitors, J. Power Sources 196 (2011) 550–558.
[2] C. Merlet, B. Rotenberg, P.A. Madden, P.L. Taberna, P. Simon, Y. Gogotsi, M. Salanne, On the molecular origin of supercapacitance in nanoporous carbon electrodes, Nat. Mater. 11 (2012) 306–310.
[3] X. Zhang, L. Ji, S. Zhang, W. Yang, Synthesis of a novel polyaniline-intercalated layered manganese oxide nanocomposite as electrode material for electrochemical capacitor, J. Power Sources 173 (2007) 1017–1023.
[4] J. Chmiola, C. Largeot, P.L. Taberna, P. Simon, Y. Gogotsi, Desolvation of ions in subnanometer pores and its effect on capacitance and double-layer theory, Angew. Chem. 120 (2008) 3440–3443.
[5] A. Davies, A. Yu, Material advancements in supercapacitors: from activated carbon to carbon nanotube and graphene, Can. J. Chem. Eng. 89 (2011) 1342–1357.
[6] S.T. Senthilkumar, B. Senthilkumar, S. Balaji, C. Sanjeeviraja, R. Kalai Selvan, Preparation of activated carbon from sorghum pith and its structural and electrochemical properties, Mater. Res. Bull. 46 (2011) 413–419.
[7] Y. Gao, Q.Y. Yue, Y.Y. Sun, J.N. Xiao, B.Y. Gao, P. Zhao, H. Yu, Optimization of high surface area activated carbon production from *Enteromorpha prolifra* with low-dose activating agent, Fuel Process. Technol. 132 (2015) 180–187.
[8] B. Xu, F. Wu, Y. Su, G. Cao, S. Chen, Z. Zhou, Y. Yang, Competitive effect of KOH activation on the electrochemical performances of carbon nanotubes for EDLC: balance between porosity and conductivity, Electrochim. Acta 53 (2008) 7730–7735.
[9] N. Liu, J. Shen, D. Liu, Activated high specific surface area carbon aerogels for EDLCs, Microporous Mesoporous Mater. 167 (2013) 176–181.
[10] J.R. Miller, R.A. Outlaw, B.C. Holloway, Graphene electric double layer capacitor with ultra-high-power performance, Electrochim. Acta 56 (2011) 10443–10449.
[11] J. Qiu, G. Wang, Y. Bao, D. Zeng, Y. Chen, Effect of oxidative modification of coal tar pitch-based mesoporous activated carbon on the adsorption of benzothiophene and dibenzothiophene, Fuel Process. Technol. 129 (2015) 85–90.
[12] C. Zhang, D. Long, B. Xing, W. Qiao, R. Zhang, L. Zhan, X. Liang, L. Ling, The superior electrochemical performance of oxygen-rich activated carbons prepared from bituminous coal, Electrochem. Commun. 10 (2008) 1809–1811.
[13] L. Sun, C. Tian, M. Li, X. Meng, L. Wang, R. Wang, J. Yin, H. Fu, From coconut shell to porous graphene-like nanosheets for high-power supercapacitors, J. Mater. Chem. A 1 (2013) 6462–6470.
[14] S.T. Senthilkumar, R.K. Selvan, J.S. Melo, C. Sanjeeviraja, High performance solid-state electric double layer capacitor from redox mediated gel polymer electrolyte and renewable tamarind fruit shell derived porous carbon, ACS Appl. Mater. Interfaces 5 (2013) 10541–10550.
[15] G.G. Stavropoulos, Precursor materials suitability for super activated carbons production, Fuel Process. Technol. 86 (2005) 1165–1173.
[16] Y. Fang, W. Dai, L. Chen, N. Ma, Facile synthesis of ordered mesoporous carbon with finger citron residue as carbon precursor, Mater. Lett. 174 (2016) 246–248.
[17] A. Kurniawan, S. Ismadji, Potential utilization of *Jatropha curcas* L. press-cake residue as new precursor for activated carbon preparation: application in methylene blue removal from aqueous solution, J. Taiwan Inst. Chem. Eng. 42 (2011) 826–836.
[18] K. Legrouri, E. Khouya, M. Ezzine, H. Hannache, R. Denoyel, R. Pallier, R. Naslain, Production of activated carbon from a new precursor molasses by activation with sulphuric acid, J. Hazard. Mater. 118 (2005) 259–263.

[19] D. Zhai, B. Li, F. Kang, H. Du, C. Xu, Preparation of mesophase-pitch-based activated carbons for electric double layer capacitors with high energy density, Microporous Mesoporous Mater. 130 (2010) 224–228.
[20] D. Zhai, B. Li, H. Du, G. Wang, F. Kang, The effect of pre-carbonization of mesophase pitch-based activated carbons on their electrochemical performance for electric double-layer capacitors, J. Solid State Electrochem. 15 (2010) 787–794.
[21] M. Wu, P. Li, Y. Li, J. Liu, Y. Wang, Enteromorpha based porous carbons activated by zinc chloride for supercapacitors with high capacity retention, RSC Adv. 5 (2015) 16575–16581.
[22] B. Xu, F. Wu, R. Chen, G. Cao, S. Chen, Y. Yang, Mesoporous activated carbon fiber as electrode material for high-performance electrochemical double layer capacitors with ionic liquid electrolyte, J. Power Sources 195 (2010) 2118–2124.
[23] D. Hulicova-Jurcakova, M. Seredych, G.Q. Lu, T.J. Bandosz, Combined effect of nitrogen- and oxygen-containing functional groups of microporous activated carbon on its electrochemical performance in supercapacitors, Adv. Funct. Mater. 19 (2009) 438–447.
[24] X.Y. Zhao, J.P. Cao, K. Sato, Y. Ogawa, T. Takarada, High surface area activated carbon prepared from black liquor in the presence of high alkali metal content, J. Chem. Eng. Jpn 43 (2010) 1029–1034.
[25] X. Huang, J.P. Cao, X.Y. Zhao, J.X. Wang, X. Fan, Y.P. Zhao, X.Y. Wei, Pyrolysis kinetics of soybean straw using thermogravimetric analysis, Fuel 169 (2016) 93–98.
[26] X.Y. Zhao, S.S. Huang, J.P. Cao, S.C. Xi, X.Y. Wei, J. Kamamoto, T. Takarada, KOH activation of a HyperCoal to develop activated carbons for electric double-layer capacitors, J. Anal. Appl. Pyrolysis 105 (2014) 116–121.
[27] L. Fuhu, C. Weidong, S. Zengmin, W. Yixian, L. Yunfang, L. Hui, Activation of mesocarbon microbeads with different textures and their application for supercapacitor, Fuel Process. Technol. 91 (2010) 17–24.
[28] X. He, P. Ling, J. Qiu, M. Yu, X. Zhang, C. Yu, M. Zheng, Efficient preparation of biomass-based mesoporous carbons for supercapacitors with both high energy density and high power density, J. Power Sources 240 (2013) 109–113.
[29] X. He, P. Ling, M. Yu, X. Wang, X. Zhang, M. Zheng, Rice husk-derived porous carbons with high capacitance by ZnCl2 activation for supercapacitors, Electrochim. Acta 105 (2013) 635–641.
[30] K. Zhang, W.L. Zhang, H.J. Choi, Facile fabrication of self-assembled PMMA/graphene oxide composite particles and their electroresponsive properties, Colloid Polym. Sci. 291 (2012) 955–962.
[31] J. Jaramillo, P.M. Ivarez, V. Gómez-Serrano, Oxidation of activated carbon by dry and wet methods, Fuel Process. Technol. 91 (2010) 1768–1775.
[32] G. Huang, W. Kang, B. Xing, L. Chen, C. Zhang, Oxygen-rich and hierarchical porous carbons prepared from coal based humic acid for supercapacitor electrodes, Fuel Process. Technol. 142 (2016) 1–5.
[33] F. Ran, X. Zhang, Y. Liu, K. Shen, X. Niu, Y. Tan, L. Kong, L. Kang, C. Xu, S. Chen, Super long-life supercapacitor electrode materials based on hierarchical porous hollow carbon microcapsules, RSC Adv. 5 (2015) 87077–87083.
[34] H. Jiang, J. Ma, C. Li, Mesoporous carbon incorporated metal oxide nanomaterials as supercapacitor electrodes, Adv. Mater. 24 (2012) 4197–4202.
[35] D. Qu, Studies of the activated carbons used in double-layer supercapacitors, J. Power Sources 109 (2002) 403–411.
[36] C. Peng, X.B. Yan, R.T. Wang, J.W. Lang, Y.J. Ou, Q.J. Xue, Promising activated carbons derived from waste tea-leaves and their application in high performance supercapacitors electrodes, Electrochim. Acta 87 (2013) 401–408.
[37] Y. Zhu, S. Murali, M.D. Stoller, K. Ganesh, W. Cai, P.J. Ferreira, A. Pirkle, R.M. Wallace, K.A. Cychosz, M. Thommes, Carbon-based supercapacitors produced by activation of graphene, Science 332 (2011) 1537–1541.
[38] W. Li, K. Yang, J. Peng, L. Zhang, S. Guo, H. Xia, Effects of carbonization temperatures on characteristics of porosity in coconut shell chars and activated carbons derived from carbonized coconut shell chars, Ind. Crop. Prod. 28 (2008) 190–198.
[39] M. Thommes, K. Kaneko, A.V. Neimark, J.P. Olivier, F. Rodriguez-Reinoso, J. Rouquerol, K.S.W. Sing, Physisorption of gases, with special reference to the evaluation of surface area and pore size distribution (IUPAC technical report), Pure Appl. Chem. 87 (2015) 1051–1069.
[40] S.T. Senthilkumar, R.K. Selvan, Y.S. Lee, J.S. Melo, Electric double layer capacitor and its improved specific capacitance using redox additive electrolyte, J. Mater. Chem. A 1 (2013) 1086–1095.
[41] Y. Guo, Z. Shi, M. Chen, C. Wang, Hierarchical porous carbon derived from sulfonated pitch for electrical double layer capacitors, J. Power Sources 252 (2014) 235–243.
[42] P. Simon, Y. Gogotsi, Materials for electrochemical capacitors, Nat. Mater. 7 (2008) 845–854.
[43] L. Ding, B. Zou, H. Liu, Y. Li, Z. Wang, Y. Su, Y. Guo, X. Wang, A new route for conversion of corncob to porous carbon by hydrolysis and activation, Chem. Eng. J. 225 (2013) 300–305.
[44] L. Wei, G. Yushin, Nanostructured activated carbons from natural precursors for electrical double layer capacitors, Nano Energy 1 (2012) 552–565.
[45] X.Y. Zhao, S.S. Huang, J.P. Cao, X.Y. Wei, K. Magarisawa, T. Takarada, HyperCoal-derived porous carbons with alkaline hydroxides and carbonate activation for electric double-layer capacitors, Fuel Process. Technol. 125 (2014) 251–257.
[46] N. Jäckel, M. Rodner, A. Schreiber, J. Jeongwook, M. Zeiger, M. Aslan, D. Weingarth, V. Presser, Anomalous or regular capacitance? The influence of pore size dispersity on double-layer formation, J. Power Sources 326 (2016) 660–671.
[47] B. Chang, D. Guan, Y. Tian, Z. Yang, X. Dong, Convenient synthesis of porous carbon nanospheres with tunable pore structure and excellent adsorption capacity, J. Hazard. Mater. 262 (2013) 256–264.
[48] M. Biswal, A. Banerjee, M. Deo, S. Ogale, From dead leaves to high energy density supercapacitors, Energy Environ. Sci. 6 (2013) 1249–1259.
[49] R. Demircakan, N. Baccile, M. Antonietti, M.M. Titirici, Carboxylate-rich carbonaceous materials via one-step hydrothermal carbonization of glucose in the presence of acrylic acid, Chem. Mater. 21 (2009) 484–490.
[50] S. Teng, G. Siegel, W. Wang, A. Tiwari, Carbonized wood for supercapacitor electrodes, ECS Solid State Lett. 3 (2014) M25–M28.
[51] K.T. Cho, S.B. Lee, J.W. Lee, Facile synthesis of highly electrocapacitive nitrogen-doped graphitic porous carbons, J. Phys. Chem. C 118 (2014) 9357–9367.
[52] B. Chang, B. Yang, Y. Guo, Y. Wang, X. Dong, Preparation and enhanced supercapacitance performance of porous carbon spheres with a high degree of graphitization, RSC Adv. 5 (2015) 2088–2095.
[53] Q. Wang, J. Yan, Y. Wang, T. Wei, M. Zhang, X. Jing, Z. Fan, Three-dimensional flower-like and hierarchical porous carbon materials as high-rate performance electrodes for supercapacitors, Carbon 67 (2014) 119–127.
[54] J. Zhao, B. Tang, J. Cao, J. Feng, P. Liu, J. Zhao, J. Xu, Effect of hydrothermal temperature on the structure and electrochemical performance of manganese compound/ordered mesoporous carbon composites for supercapacitors, Mater. Manuf. Process. 27 (2012) 119–124.
[55] M.W. Xu, L.B. Kong, W.J. Zhou, H.L. Li, Hydrothermal synthesis and pseudocapacitance properties of r-MnO_2 hollow spheres and hollow urchins, J. Phys. Chem. C 111 (2007) 19141–19147.
[56] Y. Chen, X. Zhang, D. Zhang, P. Yu, Y. Ma, High performance supercapacitors based on reduced graphene oxide in aqueous and ionic liquid electrolytes, Carbon 49 (2011) 573–580.
[57] M. Li, C. Liu, H. Cao, H. Zhao, Y. Zhang, Z. Fan, KOH self-templating synthesis of three-dimensional hierarchical porous carbon materials for high performance supercapacitors, J. Mater. Chem. A 2 (2014) 14844–14851.
[58] X. He, Z. Liu, H. Ma, N. Zhang, M. Yu, M. Wu, Shell-like hierarchical porous carbons for high-rate performance supercapacitors, Microporous Mesoporous Mater. 236 (2016) 134–140.
[59] X. He, X. Li, H. Ma, J. Han, H. Zhang, C. Yu, N. Xiao, J. Qiu, ZnO template strategy for the synthesis of 3D interconnected graphene nanocapsules from coal tar pitch as supercapacitor electrode materials, J. Power Sources 340 (2017) 183–191.
[60] V.S. Jamadade, V.J. Fulari, C.D. Lokhande, Supercapacitive behavior of electrosynthesized marygold-like structured nickel doped iron hydroxide thin film, J. Alloys Compd. 509 (2011) 6257–6261.
[61] F. Ran, K. Shen, Y. Tan, B. Peng, S. Chen, W. Zhang, X. Niu, L. Kong, L. Kang, Activated hierarchical porous carbon as electrode membrane accommodated with triblock copolymer for supercapacitors, J. Membr. Sci. 514 (2016) 366–375.
[62] X. He, N. Zhang, X. Shao, M. Wu, M. Yu, J. Qiu, A layered-template-nanospace-confinement strategy for production of corrugated graphene nanosheets from petroleum pitch for supercapacitors, Chem. Eng. J. 297 (2016) 121–127.